IEEE Access
Multidisciplinary | Rapid Review | Open Access Journal

Date of publication xxxx 00, 0000, date of current version xxxx 00, 0000.

Digital Object Identifier 10.1109/ACCESS.2017.Doi Number

Isolation Improvement of MIMO Antenna Using Novel EBG and Hair-pin Shaped DGS at 5G Millimeter Wave Band

Soumik Dey[1], Student Member, IEEE, Sukomal Dey[1], Senior Member, IEEE and Shiban K Koul[2], Life Fellow, IEEE

[1] Department of Electrical Engineering, Indian Institute of Technology Palakkad, Kerala: 678557, India
[2] Centre for Applied Research in Electronics, Indian Institute of Technology Delhi, New Delhi: 110016, India

Corresponding author: Sukomal Dey (e-mail: sukomal.iitpkd@gmail.com).

This work was supported by the Science and Engineering Research Board, Govorment of India under project no. ECR/2018/002258.

ABSTRACT This paper proposes a hybrid decoupling method based on a novel electromagnetic bandgap (EBG) structure and hair-pin shaped defected ground structure (DGS) to obtain high isolation between 2-element multiple input multiple output (MIMO) antenna at 5G millimeter wave band over 27.5–28.35 GHz. The proposed EBG designed on stacked dielectric substrates, achieves a wide frequency band-gap between 26.2–32.03 GHz (20 %). A 2 × 3 array of the EBG is arranged between two electromagnetically coupled radiating patches in order to suppress the surface wave coupling. Substrate integrated waveguide (SIW) feeding network and cavity are strategically incorporated in the antenna design for improving the radiation performance and minimizing the losses from the feed. EBG shows an average isolation improvement of 13.9 dB within 5G band as compared to unloaded MIMO antenna. The additional reduction in coupling is achieved by placing hair-pin DGS (HP-DGS) on the ground plane, resulting into maximum isolation improvement of 47.7 dB at 27.94 GHz. The prototype of the MIMO was fabricated and experimentally verified. Measured peak isolation between the antennas is obtained as 71.9 dB, having a gain of 9 dBi and front to back ratio (FTBR) of 19.8 dB. A good diversity diversity performance is also noticed for the designed MIMO with envelope correlation coefficient (ECC) of 0.00015, diversity gain (DG) of 9.99 and channel capacity loss (CCL) of 0.025 bits/Hz/sec. Later, SIW corporate feed network is designed for 4-element linear array loaded with EBG and HP-DGS to achieve higher gain and narrow beamwidth. The array was fabricated and the measured results are found in good accordance with the simulation results. The peak gain, beamwidth, and FTBR of the array are 13.3 dBi, 16.2°, and 19.97 dB respectively.

INDEX TERMS Antenna array, defected ground structure (DGS), electromagnetic bandgap (EBG), mutual coupling reduction, multiple input multiple output (MIMO)

I. INTRODUCTION

Inception of the fifth-generation (5G) wireless technology to fulfill the demands of efficient and high-speed transmission throughput requires multiple antennas at the transmitting and receiving ends [1]–[2]. To meet the requirement of space constraint in modern internet of things (IOT) based wireless gadgets antenna elements need to be densely packed. In common system circuit boards, the existence of surface wave at the air-dielectric interface gives rise to cross-talk between the closely spaced antennas. This deteriorates the channel capacity and efficiency of the MIMO system [3] and also causes scan blindness in phased array [4]. Different methods to reduce the crosstalk in MIMO / phased array can be listed as coupled line resonator [5], neutralization line [6]–[7], polarization isolator [8], capacitively-loaded loop (CLL) [9], metamaterial superstrate [10]–[12], split ring resonator (SRR) [13]–[14], EBG [15]–[22], DGS [23]–[24], and metamaterial absorber [25]. The mutual coupling problem becomes more severe at the millimeter (mm) wave transceiver system. Thick electrical thickness of the substrate at mm-wave originates the high-order surface wave modes [26]–[27]. In addition to that, space wave coupling between the array elements enhances correlation and hence reduces the scanning range and gain of the beam steerable antenna [28]. Till to date, only few attempts were made to address the coupling reduction in mm-wave

This article has been accepted for publication in a future issue of this journal, but has not been fully edited. Content may change prior to final publication. Citation information: DOI 10.1109/ACCESS.2021.3133324, IEEE Access

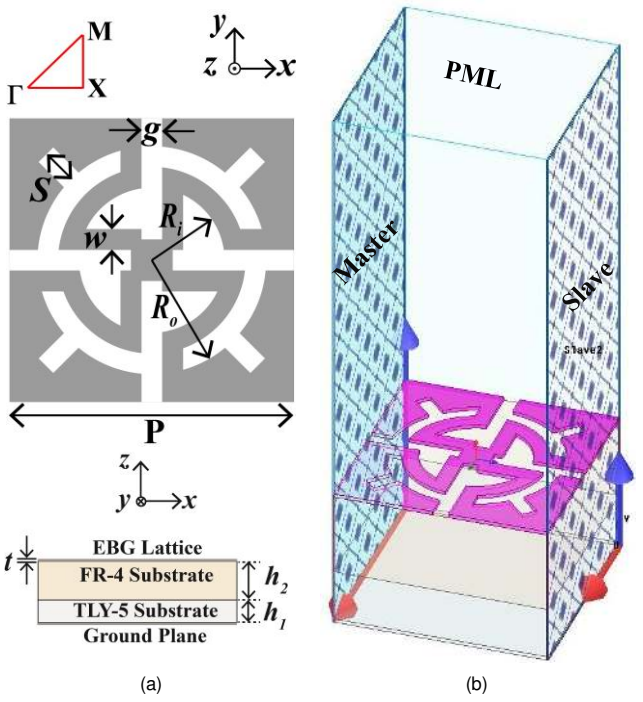

FIGURE 1. Proposed EBG unit cell (a) front and side views (b) simulation setup for the proposed unit cell to evaluate dispersion characteristics.

circuits [29]–[34]. With the growing interest in mm-wave communication, coupling needs to be controlled in the MIMO antenna with minimum increase in the design complexity. In similar works reported earlier especially at mm-wave range, methods for improving the impedance matching and radiation efficiency have not considered in the design process.

In this paper, a compact uniplanar EBG is designed following a detailed analysis based on the equivalent circuit model (ECM). A hybrid isolator based on the EBG and HP-DGS is introduced for isolation improvement between two H-plane coupled MIMO antennas. Simulation of the MIMO antenna and the EBG is performed using High-Frequency Structure Simulator (HFSS) software. Later experimental results are found consistent with the simulation results. A 4-element array loaded with EBG and HP-DGS is designed that has features of high gain, low side lobe level (SLL), and high FTBR. The salient features of the present work are (i) unique design strategy of the EBG on stacked dielectric substrates with different relative permittivities, causing high attenuation of the coupling field over a wide band (ii) EBG-DGS based hybrid isolation method that achieves highest isolation improvement of 47.7 dB at the millimeter wave range (iii) new variation of the millimeter wave MIMO antenna and 4-element linear array which integrate the SIW cavity along with proximity feeding method to obtain simultaneously wideband matching, high FTBR and limit the propagation of surface wave. Sections II describes the geometry of the proposed uniplanar EBG and ECM. The single antenna element and its simulation results are presented in section III. Schematic of the decoupled MIMO antenna and its isolation characteristics are discussed in section IV. Section V presents fabricated MIMO antenna and its measurement results, followed by state-of-the-art performance comparison. Design of SIW cavity-backed 4-element linear array is discussed in section VI. Finally, the conclusion of the work is drawn in section VII.

II. DESIGN AND ANALYSIS OF PROPOSED EBG

A. UNIT CELL GEOMETRY

EBG is a 2D periodic structure which generally classified into two types–mushroom and uniplanar based on the unit cell geometry. The second kind of configuration has the advantage of without having shorting pins which simplifies the design. EBG supports different surface wave modes with each one of the modes having different field configurations. The mode with zero cutoff frequency is called transverse magnetic (TM) mode. EBG suppresses the propagation of the surface wave within its frequency bandgap due to its high impedance surface nature and also exhibits in-phase reflection similar to a perfect magnetic conductor (PMC) surface [35]. Fig. 1 (a) shows the unit cell geometry of the proposed uniplanar EBG consists of two metal layers separated by two substrates with different dielectric constants (ε_r). The bottom metal layer acts as a ground plane. Two substrates are Taconic TLY-5 (ε_{r1} = 2.2) and FR-4 (ε_{r2} = 4.4) with loss tangent values of 0.0009 and 0.02 respectively. The two substrates have thicknesses (h_1 and h_2) of 0.51 mm and 0.8 mm. Compare with the earlier reported EBGs, the novelty of the proposed geometry is the use of two substrates with different dielectric constants. This causes multiple reflections of the surface wave at the interface between the top and bottom layers due to a change in refractive index (n). Here $n \propto \sqrt{\mu_r \varepsilon_r}$ with μ_r denotes the relative permeability with a value of 1 for the non-magnetic material. Multiple reflections may also cause destructive interference inside stacked dielectric substrates, resulting into additional attenuation of surface wave over broad frequency range. This leads to wide bandgap of the EBG. Stacking of two substrates can be considered as a composite dielectric (CD) layer having a total thickness of 1.31 mm. The effective dielectric constant (ε_{eff}) of CD layer is found as 3.45 using (1)

$$\sqrt{\varepsilon_{eff}} = \left(\frac{\sqrt{\varepsilon_{r1}} h_1 + \sqrt{\varepsilon_{r2}} h_2}{h_1 + h_2} \right) \tag{1}$$

B. DISPERSION CHARACTERISTICS

The surface wave propagation characteristic of the EBG is obtained from the dispersion diagram which is a graphical representation of wavenumber (k) against frequency (f). For a lossy medium like EBG, k exhibits a nonlinear variation with frequency. The numerical simulation of the EBG is performed using the Eigen modes solver of the HFSS imposing periodic unit cell boundary, as shown in Fig. 1 (b). The height of the radiation box is assumed five times the total thickness of the unit cell. Periodic master-slave boundaries are assigned at the walls of the radiation box along x and y axes. While the wall along the + z-axis is terminated with a perfectly matched layer (PML) boundary. The 90° rotational symmetry in the unit cell

This article has been accepted for publication in a future issue of this journal, but has not been fully edited. Content may change prior to final publication. Citation information: DOI 10.1109/ACCESS.2021.3133324, IEEE Access

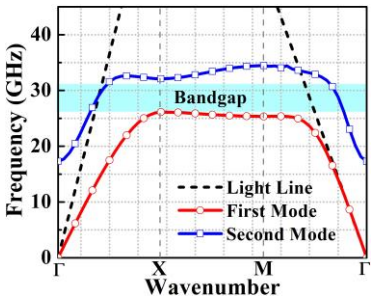

FIGURE 2. Dispersion characteristics of the proposed uniplanar EBG.

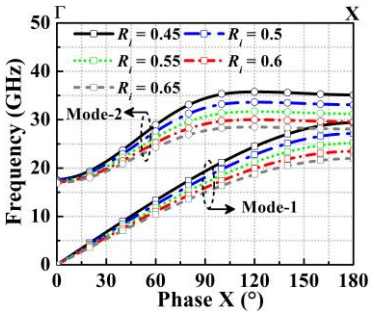

(a)

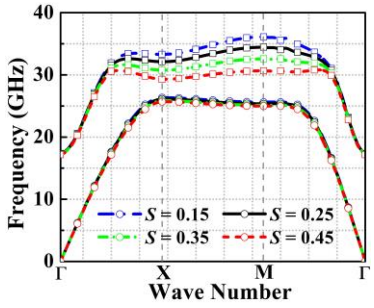

(b)

FIGURE 3. Dispersion diagram at different values of (a) R_i and (b) S.

geometry allows solving the Eigen frequencies only over the Brillouin zone triangle (Γ-X-M). Fig. 2 shows the dispersion characteristic of the proposed EBG that exhibits a frequency bandgap from 26.2 to 32.03 GHz (5.83 GHz or 20 %) between the two lowest order propagating modes. This bandgap is observed within the region covered by the light line which separates the unguided plane wave region and the guided surface wave region. The wideband bandgap of the proposed EBG is attributed to the inter-cell connection between adjacent unit cells. This enhances the total inductance (L) and increases the bandgap bandwidth (BW) which is proportional to $\sqrt{L/C}$. Here C denotes the overall capacitance of the unit cell. Final dimensions of the proposed EBG are P = 2.05, w = 0.15, g = 0.15, S = 0.25, R_i = 0.525, R_o = 0.825, t = 0.035 mm. The unit cell has periodicity of 0.19 λ_0 where λ_0 is the free space wavelength at the bandgap center frequency of 29.12 GHz.

C. PARAMETRIC ANALYSIS

The geometry of the unit cell consists of a center cross dipole whose arms are convoluted in the form of sectoral patches.

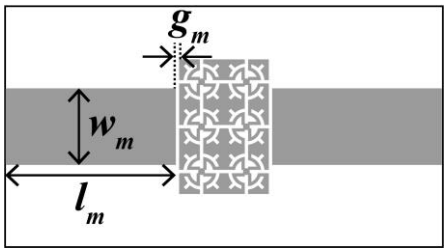

(a)

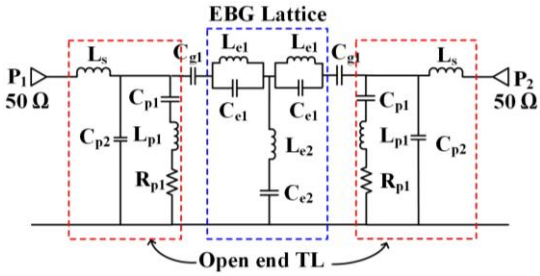

(b)

FIGURE 4. EBG loaded open ended TL (a) schematic layout (b) ECM. Parameters are l_m = 7.8, w_m = 3.5, g_m = 0.15.

Fours diagonal slits having length 'S' are included within the sectoral patches to control the BW of the frequency bandgap. The sensitivity of the frequency bandgap on the unit cell dimensions is further analyzed using parametric variations, shown in Fig. 3. Fig. 3 (a) depicts the dispersion plot against different radius (R_i) of the cross dipole over the region of Γ to X with phase variation (Phase X) from 0° to 180°. The increase in R_i causes the increase in periodicity of the unit cell and shifts the two modes towards lower frequency. The bandgap between the two modes is invariant with change in R_i, because the L and C increase in same proportions, keeping the L/C ratio same. Variation of the diagonal slit length (S) provides the bandwidth control of the EBG as illustrated in Fig. 3(b). The increase in S enhances the slot capacitance of the top metasurface. This in effect reduces the Eigen frequency of the second mode. This frequency corresponds to zero group velocity ($d\omega / d\beta = 0$) and determines the upper limit of the EBG bandgap. On contrary, the change in S does not affect the wave dispersion of the first mode. The bandgap of the proposed EBG decreases with an increase in S due to an increase in capacitance. The fractional bandwidth (FBW) of the bandgap changes from 23 % to 8.24 % when S varies from 0.15 to 0.45 mm.

C. Equivalent Circuit for Symmetric Transmission Line

Another method of validating bandgap of the EBG is based on the symmetric transmission line (TL) technique, shown in Fig. 4 (a). Two open-ended TLs with characteristics impedance of 50 Ω are facing each other with a gap of 4.4 mm between them. Two lines act as launcher and receptor of the signal. The placing of 2 × 3 EBG unit cells in between the TLs alters the transmission coefficient (S_{21}) of the structure. To obtain a physical insight into the proposed EBG, an ECM of the EBG is designed as illustrated in Fig. 4 (b). The open-end TL is

This article has been accepted for publication in a future issue of this journal, but has not been fully edited. Content may change prior to final publication. Citation information: DOI 10.1109/ACCESS.2021.3133324, IEEE Access

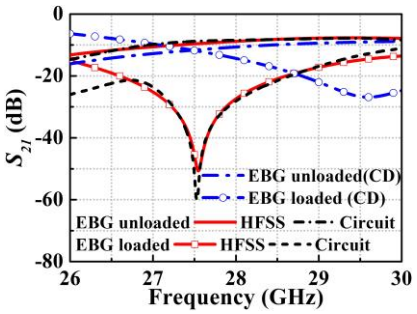

(a)

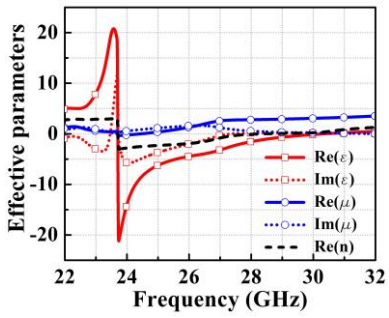

(b)

FIGURE 5. (a) Simulated transmission coefficient of the EBG loaded and unloaded open-ended TLs (b) effective medium parameters of the EBG. CD signifies composite dielectric

represented as a series inductance (L_s) and shunt capacitance (C_{p2}). At mm-wave fringing from the edges of the TL are taken into consideration by placing additional series resonance (R_{p1} - L_{p1} - C_{p1}) in shunt [36]. For open-end TL, circuit parameter values are analytically found using (2)-(6) with inductance, capacitance, and resistance are in nH, pF, and Ω units [36].

$$L_s = 0.2l_m\left[\ln\left(\frac{2l_m}{w_m+h}\right)+0.5+0.2235\left(\frac{w_m+h}{l_m}\right)\right] \quad (2)$$

$$L_{p1} = 1.575Z_0h\left[0.008285\tanh\left(0.5665\frac{w_m}{h}\right)+0.0103\right] \quad (3)$$

$$C_{p1} = 1.575\frac{h}{Z_0}\left[6.832\tanh\left(0.0109\frac{w_m}{h}\right)+0.91\right] \quad (4)$$

$$C_{p2} = 1.575\frac{h}{Z_0}\left[1.125\tanh\left(1.358\frac{w_m}{h}\right)-0.315\right] \quad (5)$$

$$R_{p1} = 1.024Z_0\tanh\left(2.025\frac{w_m}{h}\right) \quad (6)$$

Here $h = h_1 + h_2$ is the total profile height. The gap capacitance (C_{g1}) is determined from even and odd mode capacitors (C_e and C_o) using (7) [36]

$$C_{g1} = 0.5C_o - 0.25C_e \quad (7)$$

The weak coupling between the widely spaced TLs causes a small value of C_g. The estimated values of circuit parameters are: L_s = 1.98 nH, L_{p1} = 2.06 nH, C_{p1} = 0.0366 pF, C_{p2} = 0.0359 pF, C_{g1} = 0.0034 pF and R_{p1} = 29.18 Ω. In the ECM, the EBG unit cells are configured as a T network with a series branch consists of a parallel resonant circuit (L_{e1}-C_{e1}), and the shunt branch is represented by a series resonance (L_{e2}-C_{e2}). In the series resonance inductance L_{e2} occurs due to induced current on the bottom ground plane, forming a current loop between top and bottom layers. This current couples with the magnetic field of the surface wave. The fringing field at the edges of slots in the top metasurface and the overlapping area between the two metal layers contribute to the series and shunt capacitances in the ECM. The circuit parameter values of EBG are obtained in the Advanced design system (ADS) using the curve fitting technique. The final values are: L_{e1} = 3.82 nH, L_{e2} = 10.25 nH, C_{e1} = 0.0087 pF, C_{e2} = 0.073 pF. Fig. 5 (a) shows S_{21} between the two open-end TLs without and with EBG loading in the middle. The S_{21} of ECM is obtained in ADS and the result shows a close match with HFSS simulation. Over frequency bandgap of the EBG, S_{21} is significantly attenuated with maximum suppression centers at 27.5 GHz. To illustrate the advantage of the stacked dielectric substrates, the open ended TLs with and without EBG loading are simulated on CD material having height of 1.31 mm and uniform dielectric constant 3.45. The magnitude of S_{21} is suppressed by 24.2 dB more for EBG loaded open end TL on the stacked dielectric materials as compared to the same on CD layer.

TABLE I
COMPARISON OF THE PROPOSED EBG WITH PREVIOUS REPORTED WORKS

Ref.	Center Freq. (GHz)	Bandgap GHz (FBW)	Periodicity (λ_0)	Thickness (λ_0)	Type
[16]	5.63	0.58 (10.3 %)	0.1	0.029	Mushroom
[18]	5.125	0.45 (8.78 %)	0.143	0.017	Uniplanar
[19]	6.472	1.153 (17.8 %)	0.324	0.032	Uniplanar
[29]	61.95	6.3 (10.17 %)	0.047×0.202	0.103	Uniplanar
Proposed EBG	29.12	5.83 (20 %)	0.19	0.127	Uniplanar

Effective medium parameters of the EBG are also found from the scattering parameters. The medium permittivity (ε) and permeability (μ) are related to refractive index n and impedance Z by equations $\varepsilon = n / Z$ and $\mu = n Z$ where Z and n are obtained from S_{11} and S_{21} using (8) and (9) [37]

$$Z = \sqrt{\frac{(1+S_{11})^2 - S_{21}^2}{(1-S_{11})^2 - S_{21}^2}} \quad (8)$$

$$e^{jnk_0h} = \frac{S_{21}}{1-S_{11}(Z-1)/(Z+1)} \quad (9)$$

Fig. 5 (b) shows the medium parameters of the EBG in which real component of ε is negative from 23.72–30.36 GHz. The real part of the refractive index $n = \sqrt{\varepsilon\mu}$ are found to be close to zero over the 5G operating band. This confirms that the designed EBG behaves as zero index metamaterial.

Performance of the proposed EBG is compared with the reported mushroom and uniplanar EBGs, shown in Table I. The unit cell in [29] also operates in mm-wave frequency, but the EBG in this paper possesses wider bandwidth. Besides asymmetric unit cell geometry of [29], causes the bandgap to be polarization sensitive.

This article has been accepted for publication in a future issue of this journal, but has not been fully edited. Content may change prior to final publication. Citation information: DOI 10.1109/ACCESS.2021.3133324, IEEE Access

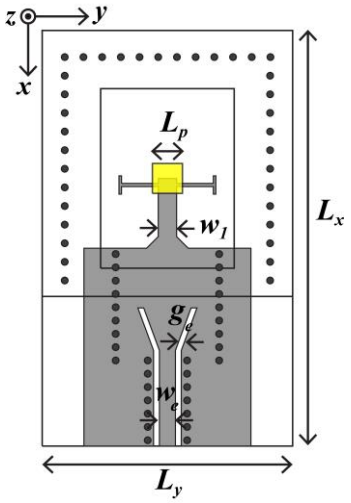

FIGURE 6. Geometry of the proposed SIW cavity-loaded proximity feed patch antenna with T-shaped stub for impedance matching.

III. SIW CAVITY LOADED PATCH ANTENNA

A. ANTENNA GEOMETRY

Fig. 6 presents the schematic of the patch antenna loaded with SIW cavity. The radiating square patch of the antenna having length L_p is excited with an electromagnetically coupled or proximity feeding method. Here instead of directly providing the signal excitation at the microstrip feed, a SIW based transition is made at the input section. The reason for this feeding arrangement is explained later. The microstrip feed with the SIW transition is printed on Taconic TLY-5 having a thickness of 0.51 mm. The substrate FR-4 with a height of 0.8 mm is used for radiating square patch and the SIW cavity with a rectangular aperture. Three sides of the cavity are enclosed by periodically arranged shorting pins which are perforated through the two substrates. Via diameter is used as 0.4 mm with a periodicity of 1 mm. A pair of 'T' shaped stubs is placed symmetrically on both sides of the microstrip feed to achieve broadband impedance matching. The length and width of the stubs are determined through a parametric analysis in HFSS. Radiating patch of the antenna is located at the open end of the microstrip feed. The wave radiates from the open end of the microstrip line and capacitively couples with the top radiating patch. This capacitance causes impedance mismatch of the antenna, which is balanced through the inductance provided by the T-shaped stubs. The two stubs are located at a distance of 0.3 mm from the open end of the microstrip line. The final design parameters are L_x = 25, L_y = 15, L_p = 1.8, w_1= 1.1, g_e = 0.35, w_e = 0.96. All units are in millimeters.

B. EQUIVALENT CIRCUIT AND SIMULATION RESULTS

The equivalent circuit of the proposed antenna is shown in Fig. 7 (a). The proximity feed patch without SIW cavity is modelled here to keep the analysis simple. In the circuit, radiating patch is represented by a parallel resonator (R_a-L_a-C_a). The fringing of the electric field from the radiating edges

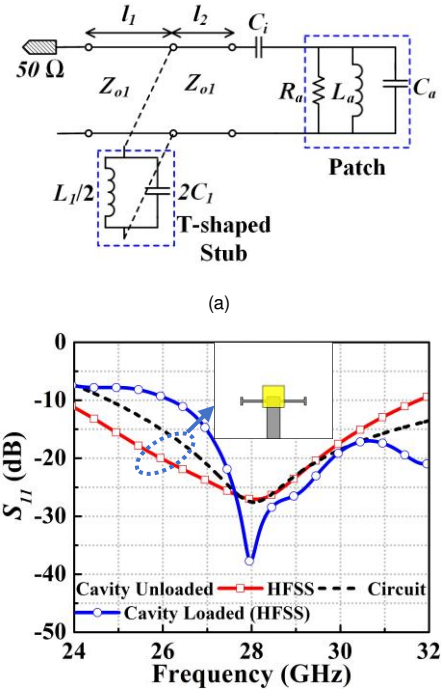

FIGURE 7. (a) Equivalent circuit of the proximity feed antenna unloaded with SIW cavity (b) simulated reflection coefficient.

causes an increase in length of the patch. This additional length (ΔL) is taken into account to determine the initial values of inductance (L_a) and capacitance (C_a). The value of ΔL is obtained using (10) [38]

$$\Delta L = 0.412 \frac{\left(\varepsilon_{eff} + 0.3\right)\left(\frac{L_p}{h} + 0.264\right)}{\left(\varepsilon_{eff} - 0.258\right)\left(\frac{L_p}{h} + 0.8\right)} \tag{10}$$

The pair of T-shaped stubs is modeled as a parallel resonator with inductance L_1 and capacitance C_1. Two sections of transmission lines having lengths l_1 and l_2 and characteristics impedances Z_{o1} are used to represent the microstrip feed line. Here (l_1 + l_2) is the total length of the feed, which has a value of 3.5 mm. The capacitance C_a of the patch is determined from the parallel plate capacitor equation. While the C_1 is obtained using (11) for an open circuit TL theory

$$C_1 = \tan \beta l_s / 2\pi f Z_{02} \tag{11}$$

Here Z_{o2} = 122.5 Ω is the characteristics impedance of the stub for the width of 0.17 mm. The stub has an effective length (l_s) of 2.73 mm. Inductances L_1 and L_a of the stub and patch are obtained using (12) by substituting corresponding length (l), width (w), metal thickness (t) in millimeters [39].

$$L(nH) = 0.2l\left[\ln\left(\frac{l}{w+t}\right) + 1.193 + 0.2235\left(\frac{w+t}{l}\right)\right] \tag{12}$$

In Fig. 7 (a) C_i denotes the coupling capacitance between the open end of the microstrip feed and the square patch and R_a signifies the radiation resistance of the antenna. The values

This article has been accepted for publication in a future issue of this journal, but has not been fully edited. Content may change prior to final publication. Citation information: DOI 10.1109/ACCESS.2021.3133324, IEEE Access

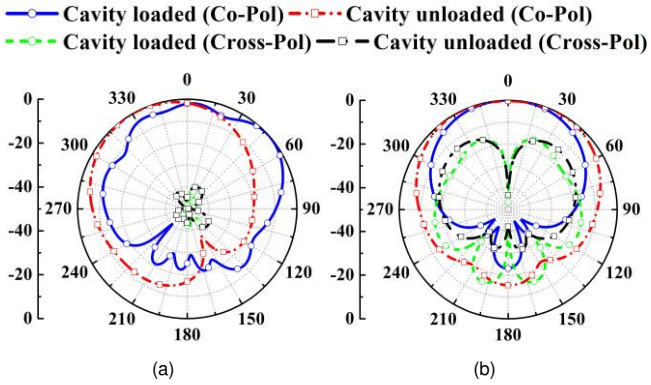

FIGURE 8. Simulated radiation patterns of the proximity feed antenna loaded with and without SIW cavity at 28 GHz in (a) E-plane (b) H-plane.

of both parameters (R_a and C_i) are found using the curve fitting approach. The equivalent circuit of the antenna is simulated using ADS and the reflection coefficient (S_{11}) is depicted in Fig. 7 (b). Full wave simulation of the proximity feed antenna without the SIW cavity is performed in HFSS. A good correlation is seen between the circuit simulated and HFSS simulated S_{11}. The antenna exhibits wideband impedance matching over the entire frequency sweep. Simulated S_{11} of the proposed SIW cavity-loaded antenna is presented in Fig. 7 (b). This single antenna element shows a resonance dip at 28 GHz with a return loss of 38 dB. Within the 5G frequency range (27.5–28.35 GHz) impedance matching is > 20 dB. Simulated 2D radiation patterns of the proposed single element antenna loaded with and without SIW cavity are illustrated in Fig. 8. The radiation patterns of the proposed antenna loaded with SIW cavity show significant improvement in FTBR in both principal planes-E and H, when compared with unloaded reference antenna. The antenna shows broadside radiation with FTBR of 22.3 dB which is more than 6.85 dB relative to the reference patch antenna. The antenna beamwidths become narrow after being loaded with the SIW cavity which also causes an improvement in antenna gain. The peak realized gain of the reference and that of the SIW cavity-loaded antenna are 4.6 dBi and 6.7 dBi respectively.

IV. MUTUAL COUPLING REDUCTION

A. H-PLANE COUPLED MIMO ANTENNA

The wideband bandgap property of the proposed EBG as described in section II is utilized for mutual coupling reduction between mm-wave antennas in 5G MIMO, depicted in Fig. 9. The antenna elements are excited using proximity feed method with electromagnetic (EM) wave is guided through SIW based transition. The incorporation of SIW which is a planar form of rectangular waveguide ensures high isolation at the input ports and diminishes the radiation leakage losses from the circuit. Two antennas can transmit and receive the EM waves independently and make a 2-element MIMO antenna. The proposed MIMO antenna consists of two substrates, having a SIW feed network built

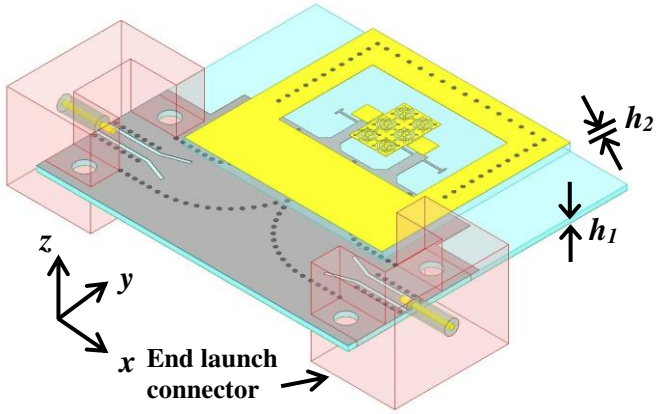

FIGURE 9. Isometric view of the proposed 2-element MIMO antenna with EBG and HP-DGS used for coupling reduction.

on Taconic TLY-5 (height h_1 = 0.51 mm) and the antennas with EBG on FR-4 material (height h_2 = 0.8 mm). At input sections of the network grounded coplanar waveguide to SIW transition is designed to facilitate the measurement. Two 2.92 mm end launch connectors from Southwest are attached with the input ports. At the output of SIW, EM wave is directly coupled from the open end of microstrip line to the radiating patches. In the proposed MIMO both radiating patches are enclosed within the SIW cavity. This improves the radiation patterns of the antenna and increases the FTBR. Fig. 10 shows the schematics of three metal layers of the proposed MIMO antenna. The first two layers are the DGS incorporated ground plane and SIW feeding, printed on two sides of Taconic TLY-5 substrate. The third metal layer is printed on a single side of FR-4 substrate. It consists of two patch antennas with symmetrically placed 2 × 3 EBG unit cells in the middle. Two antennas are H-plane coupled with the center to center spacing (d) between them is 6.2 mm or 0.58 λ_0, where λ_0 is wavelength at 28 GHz.

B. SIMULATION RESULTS

Simulated return loss and isolation characteristics of the MIMO are depicted in Fig. 11. The reference MIMO (without EBG-DGS) exhibits resonance at 28.04 GHz and shows impedance matching > 21.6 dB over 27.5–28.35 GHz, assigned for 5G application by Federal Communications Commission (FCC). Placing of EBG unit cells in the middle of two antennas reduces the coupling field. The maximum improvement in isolation is observed at 27.5 GHz (value of 23.4 dB) with an average enhancement in $|S_{21}|$ is 13.9 dB over the 5 G range. It is observed in simulation that with change in physical parameters (S and R_i) of the proposed EBG, the frequency dip in S_{21} shifts toward lower frequency away from the 5G operating range. Also the mutual coupling can not be reduced beyond a certain limit with only the EBG loading. Isolation between the antennas is further improved by placing an HP-DGS in the ground plane. DGS is symmetrically placed underneath the EBG as shown in Fig. 10 (a). The design parameters and the distance (P_y) of the DGS are optimized to

This article has been accepted for publication in a future issue of this journal, but has not been fully edited. Content may change prior to final publication. Citation information: DOI 10.1109/ACCESS.2021.3133324, IEEE Access

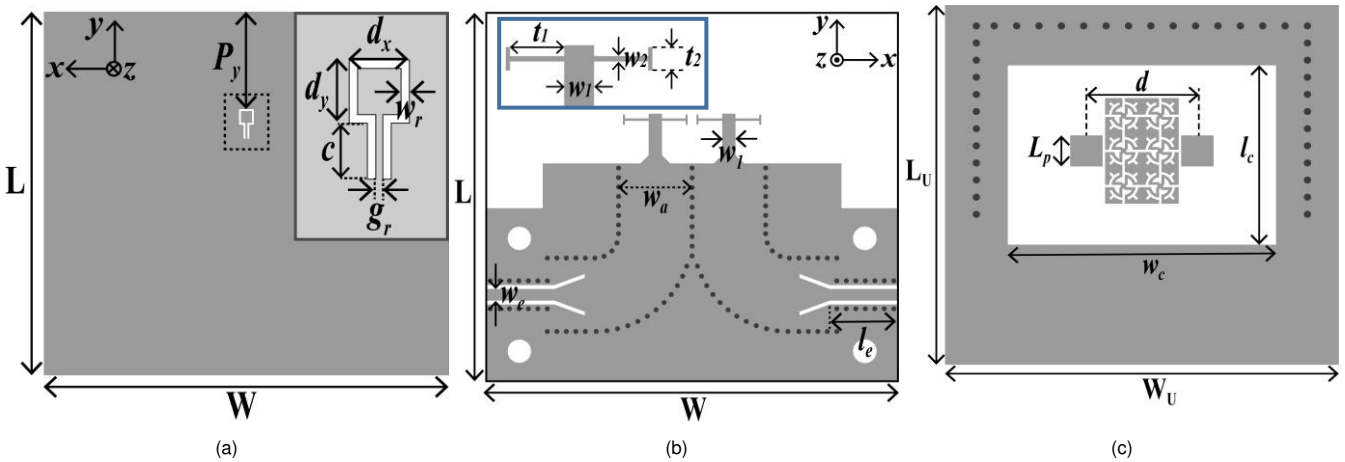

FIGURE 10. Layout of the proposed decoupled MIMO array (a) bottom ground plane with inset shows hair-pin DGS (b) middle layer consists of SIW feed (c) top layer comprises of EBG loaded antennas enclosed by SIW cavity. Parameters are L = 31.1, W = 34.7, L_u = 21, W_u = 22, w_a = 6.2, l_c = 10.5, w_c = 15, L_p = 1.8, P_y = 8.3, C = 1.2, d_x = 1.3, d_y = 1.35, w_r = 0.18, g_r = 0.15, t_1 = 2, t_2 = 0.85, w_1 = 1.1, w_2 = 0.19, l_e = 5.8, w_e = 0.96, d = 6.2.

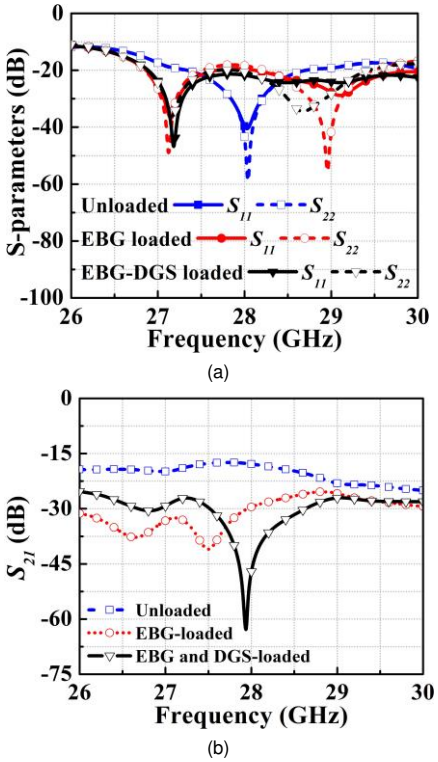

FIGURE 11. Simulated (a) reflection and (b) transmission coefficients of the proposed MIMO antenna without and with decoupling elements.

achieve maximum isolation at 28 GHz. The proposed EBG-DGS based hybrid decoupling method shows an improvement in $|S_{21}|$ of 47.7 dB at 27.94 GHz relative to the reference array. The average in band isolation of the MIMO antenna with only EBG loading is 31.9 dB while that after loading with EBG-DGS is 39.2 dB. Fig 12 shows the simulated radiation pattern of the 5G MIMO antenna in two principal planes (E and H) at frequency 28 GHz. The loading of EBG and HP-DGS hardly causes any change in radiation patterns in both planes. Placing of decoupled MIMO antenna within SIW cavity results in high FTBR with simulated maximum value is 26.1 dB. Isolation

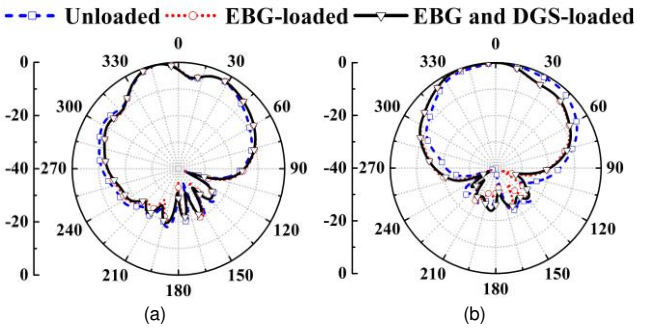

FIGURE 12. Simulated radiation patterns of the MIMO antenna at 28 GHz without and with decoupling elements (a) E-plane (b) H-plane.

improvement between the radiating patches can be explained physically from coupling current between the patches. Fig. 13 shows the surface current variation of the EBG-DGS unloaded and loaded MIMO antenna with the left side antenna being excited while the right side antenna is terminated with 50 Ω load impedance. A significant amount of current is coupled from the left patch to the right patch in the unloaded reference MIMO. On contrary for decoupled MIMO antenna, majority of the current is trapped by the EBG unit cells. Also, polarization of the coupling field in the right patch is rotated by 90°, which leads to a significant improvement in isolation. Electric field magnitudes on the ground planes of the unloaded reference MIMO and HP-DGS loaded MIMO are illustrated in Fig. 14. Considerable amount of the electric field is coupled from port 1 (left) to port 2 (right) due to low isolation between the antennas. It is worth mentioning that the inclusion of DGS additionally suppress the coupling field in the ground plane at the location of second antenna on the right.

C. DIVERSITY PERFORMANCE OF THE MIMO

The parameters which are commonly used to describe the diversity of the MIMO are envelope correlation coefficient (ECC) and diversity gain (DG). Low correlation between the antenna elements is needed for the MIMO system, which can be analyzed using ECC. In practice, ECC should be < 0.5 to

This article has been accepted for publication in a future issue of this journal, but has not been fully edited. Content may change prior to final publication. Citation information: DOI 10.1109/ACCESS.2021.3133324, IEEE Access

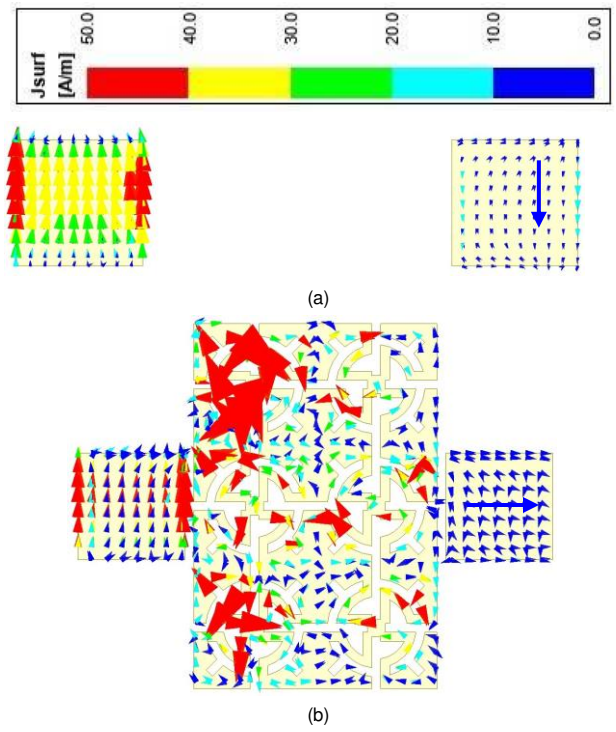

FIGURE 13. Surface current distribution on patch surface at 27.94 GHz (a) unloaded reference MIMO (b) EBG DGS loaded MIMO.

ensure high channel capacity or a good diversity performance. Two common methods of determining the ECC are based on scattering parameters and radiating fields. ECC (ρ_e) obtained using the S-parameters has less accuracy for antenna radiation efficiency < 90 %. It is preferable to estimate the ECC from far-field radiation pattern using (13) [40]

$$\rho_e = \frac{\left|\iint_{4\pi} \overrightarrow{F}_1(\theta,\varphi)^* . \overrightarrow{F}_2(\theta,\varphi)^* d\Omega\right|^2}{\iint_{4\pi}\left|\overrightarrow{F}_1(\theta,\varphi)\right|^2 d\Omega \times \iint_{4\pi}\left|\overrightarrow{F}_2(\theta,\varphi)\right|^2 d\Omega} \tag{13}$$

Here $\overrightarrow{F}_1(\theta,\varphi)$ represents the radiation field pattern of the antenna. Fig. 15 shows ECC of the proposed MIMO antenna loaded with and without EBG-DGS. Although the value of ECC increases for decoupled MIMO antenna as compared to the unloaded MIMO, the change is insignificant. At 28 GHz, ECC of the decoupled MIMO is 0.00015. The low value of ECC results in good DG of the antenna which is obtained as 9.99 using the relation $DG = 10\sqrt{1-|ECC|^2}$.

V. EXPERIMENTAL RESULTS OF MIMO ANTENNA

A prototype of the proposed MIMO antenna is fabricated and experimentally tested to validate the simulation results. Fig. 16 shows the photograph of the fabricated MIMO loaded with EBG and HP-DGS. Two substrates are bonded together using a thin layer of epoxy resin. The total size of the MIMO antenna is 34.7 × 31.1 × 1.31 mm^3. Scattering parameters of the antenna are tested using Keysight N5224B Vector Network

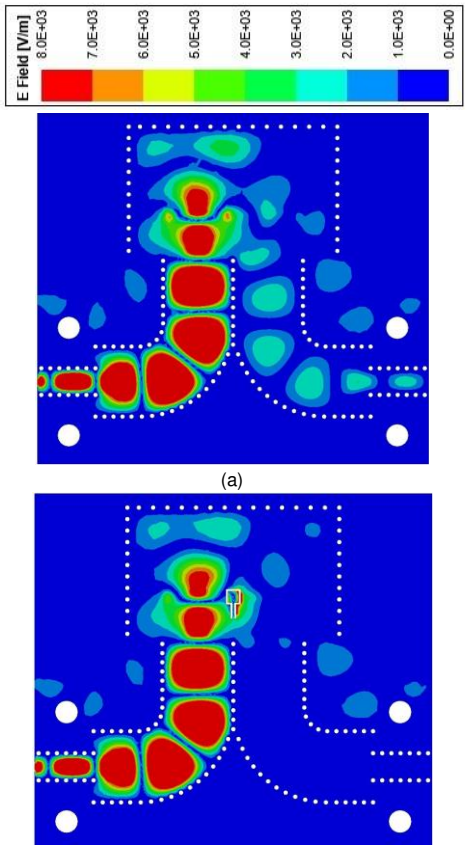

FIGURE 14. Electric field magnitude on the ground plane at 28 GHz (a) unloaded reference MIMO (b) EBG DGS loaded MIMO.

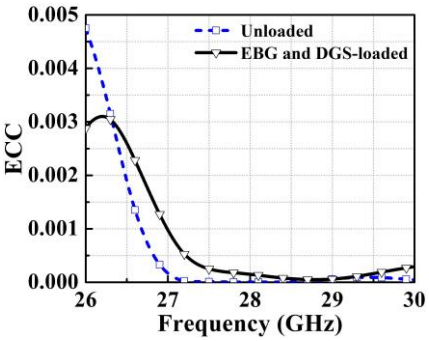

FIGURE 15. ECC of the MIMO calculated from farfield radiation patterns.

Analyzer (VNA). The radiation pattern and gain of the MIMO antenna are measured inside an anechoic chamber at IIT Palakkad using measurement setup shown in Fig. 17. Double ridged broadband horn antenna operating between 10 to 40 GHz is used as a transmitting antenna whose distance from the AUT (antenna under test) is 30 cm to satisfy farfield condition. Fig. 18 depicts the measured reflection and transmission coefficients of the proposed MIMO, with results are compared with simulation. The little discrepancy occurs due to fabrication imperfection and the presence of a thin boding layer in between the stacked dielectric substrates, resulting into change in effective dielectric constant. Measured $|S_{11}|$ and $|S_{22}|$ are > 17.4 dB within the 5G range. A dip in measured $|S_{21}|$

This article has been accepted for publication in a future issue of this journal, but has not been fully edited. Content may change prior to final publication. Citation information: DOI 10.1109/ACCESS.2021.3133324, IEEE Access

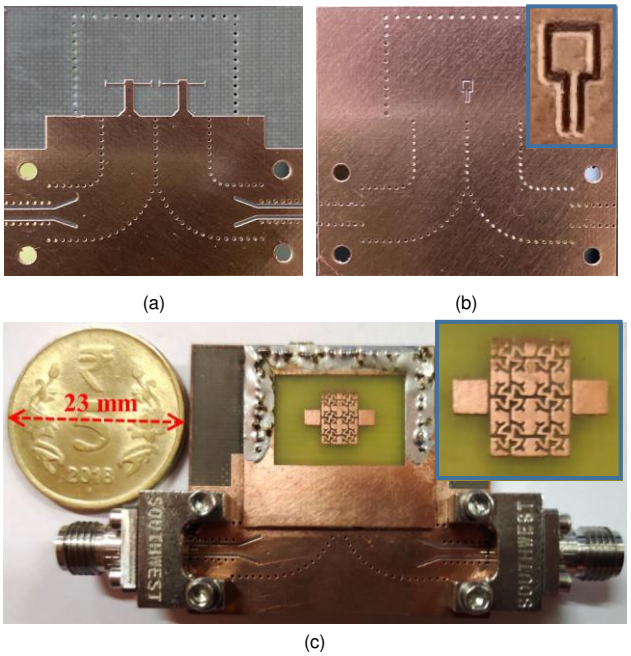

FIGURE 16. Photographs of SIW feed network (a) top view (b) bottom view (inset shows HP-DGS on backside ground plane) (c) photograph of EBG-DGS loaded MIMO antenna (inset shows the radiating patches with EBG unit cells).

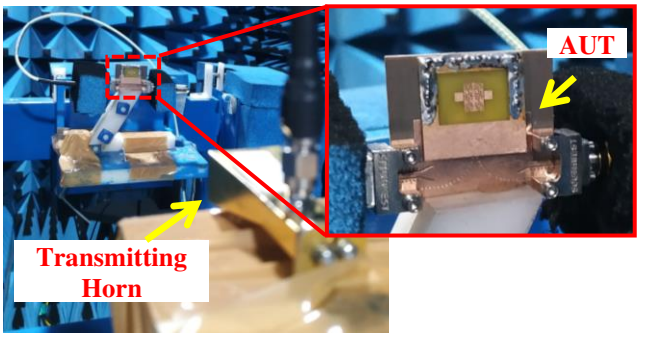

FIGURE 17. Radiation pattern and gain measurement setup inside anechoic chamber (inset shows the fabricated prototype of EBG-DGS loaded MIMO antenna).

occurs at 27.76 GHz which is shifted to lower frequency compared to the simulated response. Isolation characteristic closely follows simulated $|S_{21}|$. Maximum values of $|S_{21}|$ are 71.9 dB in measurement and 65.4 dB in simulation. Within the mm-wave 5G operating range in band isolation is > 32.7 dB. The tolerance of reflection coefficient on the presence of thin layer of air having height (h_{air}) between two substrates can be further analyzed in simulation. Fig. 19 shows that increase in air thickness causes shift in resonance frequency towards lower frequency. The above result is consistent with the measured reflection coefficient of the MIMO antenna.

While measuring the radiation patterns one of the antennas is matched terminated with 50 Ω broadband load. The E and H plane patterns at three frequencies 27.75, 28, and 28.25 GHz inside 5G range are measured and compared with the simulated results, as shown in Fig. 20. Measured radiation patterns are found consistent with simulated results. Patterns

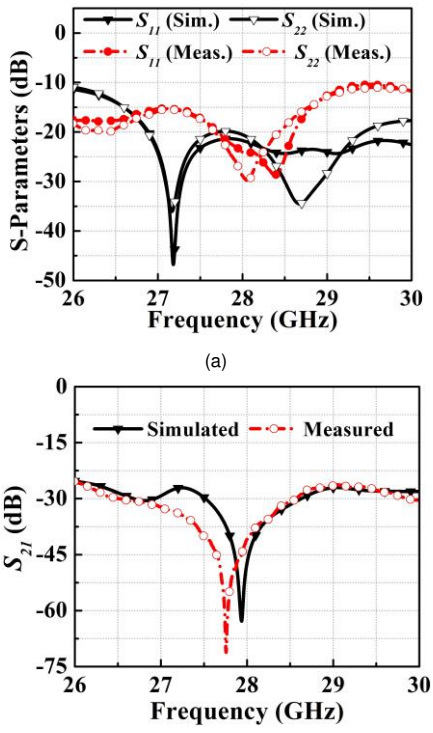

FIGURE 18. Simulated and measured (a) return loss and (b) isolation characteristics of the decoupled MIMO antenna.

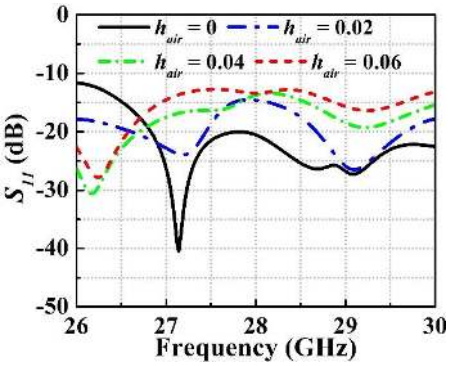

FIGURE 19. Simulated reflection coefficient of the EBG-DGS loaded MIMO antenna at different air spacer height.

exhibit a boreside radiation in both principal planes. FTBR has a maximum measured value of 19.8 dB, which is little lower than the simulated value. The gain of the decoupled MIMO antenna is also measured using gain comparison method. In this method power received by the AUT is compared with that received by standard gain horn antenna. Fig. 21 presents the simulated and measured gain of the MIMO antenna within 5G operating range. At frequency 28 GHz, the measured peak gain is obtained as 9 dBi against the simulated value of 9.3 dBi. At high frequency measured gain decreases from the simulated value. This can be attributed to an increase in losses due to radiation leakages and higher coupling between the antenna elements. Fig. 22 shows the simulated and measured total efficiency of the antenna. Wheeler cap method is realized to experimentally determine the efficiency of the antenna. The

This article has been accepted for publication in a future issue of this journal, but has not been fully edited. Content may change prior to final publication. Citation information: DOI 10.1109/ACCESS.2021.3133324, IEEE Access

TABLE II
PERFORMANCE COMPARISON OF THE PROPOSED WORK WITH PREVIOUSLY REPORTED MUTUAL COUPLING REDUCTION TECHNIQUES

Ref Year	[5] 2017	[8] 2016	[13] 2016	[14] 2015	[22] 2017	[24] 2016	[25] 2020	[30] 2019	[31] 2018	[32] 2017	[33] 2019	[34] 2017	This work
Freq. (GHz)	3.5	5.8	3.6	2.46	4.9	2.3	5.5	60	25	28	28	60	28
Method	Coupled line resonator	Polarization conversion isolator	Slot combined CSRR	1D EBG + SRR	EBG + DGS	Fractal DGS	Absorber	Hybrid isolator	CSRR	Meta-surface	Metal strip	FSS wall + DGS	EBG + DGS
Peak Isolation (dB)	40	32.8	52	53.7	35	60	43.71	49	55	49.8	24	36	71.9
In Band Isolation (dB)	20	25	35	14	22	32	23	29	32	35	22	27	32.7
Improvement in $\|S_{21}\|$ (dB)	26.2	22.3	27	42.1	22	37	12.41	25	31.8	20.12	12	21.5	47.7
Gain (dBi)	6.25	< 5	3.59	2.57	< 5	5	7.74	8.1	NA	17.9	8	NA	9
Efficiency (%)	87	60	NA	82	75	96	68.03	69	NA	85	NA	90 %	81.9
FTBR (dB)	16	13	20	9.3	10	9	15.2	11	NA	20	< 10	10	19.8
ECC	NA	NA	NA	0.002	0.002	–175 dB	0.05	NA	NA	NA	0.013	5×10^{-6}	0.00015
Element Spacing (λ_0)	0.29	0.39	0.36	0.19	0.36	0.38	0.55	0.5	0.67	1.96	0.82	0.5	0.58

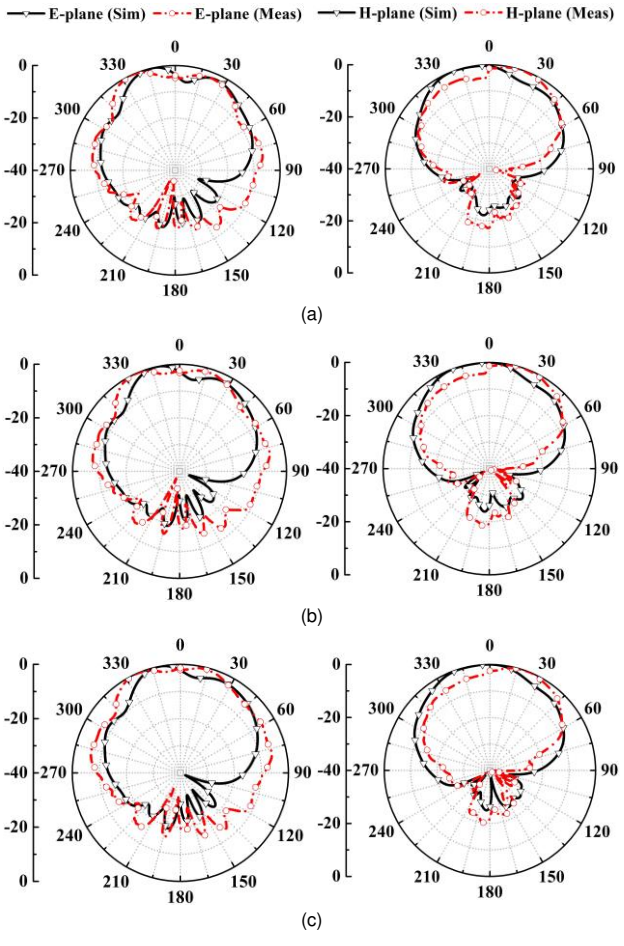

FIGURE 20. Simulated and measured E and H plane radiation patterns of the EBG DGS loaded MIMO antenna at (a) 27.75 GHz (b) 28 GHz (c) 28.25 GHz.

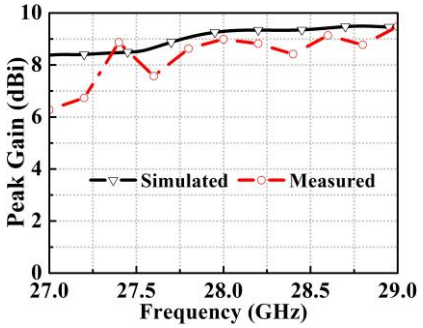

FIGURE 21. Simulated and measured gain of the EBG-DGS loaded MIMO antenna.

antenna is placed inside a cylindrical cavity made of thin layer of aluminium foil. The reflection coefficients of the antenna are measured inside the cavity and also in the outside free space. The two reflection coefficients are denoted as S_{11}^{WC} and S_{11}^{FS} respectively from which the efficiency (η) is found using the relation (14) [41]

$$\eta = 1 - \frac{\left(1 - S_{11}^{FS}\right)\left(1 + S_{11}^{WC}\right)}{\left(1 + S_{11}^{FS}\right)\left(1 - S_{11}^{WC}\right)} \tag{14}$$

At 28 GHz the simulated and measured values of η are close to 82 % while that over the 5G operating band is > 73.4 %.

In MIMO system, channel capacity signifies the maximum data rate for reliable transmission of information between transmitter and receiver. Channel capacity usually increases with increase in number of antennas. The mutual coupling between the antennas causes losses in the channel capacity. The CCL is found from the correlation matrix (ψ^k) using (15) [42]

$$CCL = -\log_2 \det\left(\psi^k\right) \tag{15}$$

This article has been accepted for publication in a future issue of this journal, but has not been fully edited. Content may change prior to final publication. Citation information: DOI 10.1109/ACCESS.2021.3133324, IEEE Access

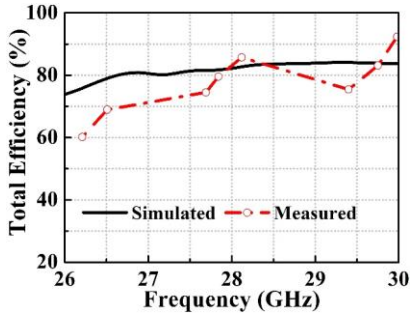

FIGURE 22. Simulated and measured efficiency of the MIMO antenna loaded with EBG and DGS for coupling reduction.

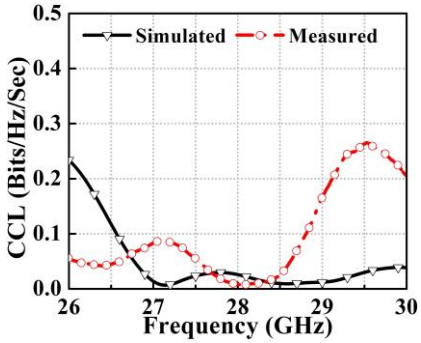

FIGURE 23. Simulated and measured CCL of the EBG DGS loaded MIMO antenna.

Elements of coupling matrix $\psi^k = \begin{bmatrix} \rho_{11} & \rho_{12} \\ \rho_{21} & \rho_{22} \end{bmatrix}$ is related to the S- parameters using (16) [42]

$$\rho_{ii} = 1 - \left(|S_{ii}|^2 + |S_{ij}|^2\right), \rho_{ij} = -\left(S_{ii}^* S_{ij} + S_{ji}^* S_{jj}\right) \quad (16)$$

for $i, j = 1$ or 2 . Acceptable value of CCL is < 0.4 bits/Hz/sec for the MIMO system. The simulated and measured CCL of the proposed MIMO antenna are shown in Fig. 23. The values of CCL are 0.025 bits/Hz/sec and 0.01 bits/Hz/sec as obtained from the simulated and measured S-parameters.

Performance of the proposed hybrid isolation improvement method is compared with other related works at microwave and mm-wave frequency, shown in Table II. The methods reported in [14], [22], and [34] also incorporate hybrid decoupling technique similar to present work, but the proposed work has the advantage of higher isolation improvement among previous reported works. The value of ECC is also found lower than all reported works except [34]. As compared to mm-wave MIMO in [30]–[34], present work shows major improvement in $|S_{21}|$ with a comparable antenna spacing. However, the gain in [32] is higher than the proposed MIMO antenna. The antenna element used in [32] is an antipodal Vivaldi with Fermi tapered slot that incurs more design complexity and having a larger footprint.

VI. SIW CAVITY BACKED 4-ELEMENT LINEAR ARRAY

A. Design of Linear Array

A SIW cavity-backed 4-element linear array is designed to illustrate the effect of the hybrid decoupling method on the array performance. The array is fed with a 4-way SIW power divider. Radiating patches are proximity coupled with output

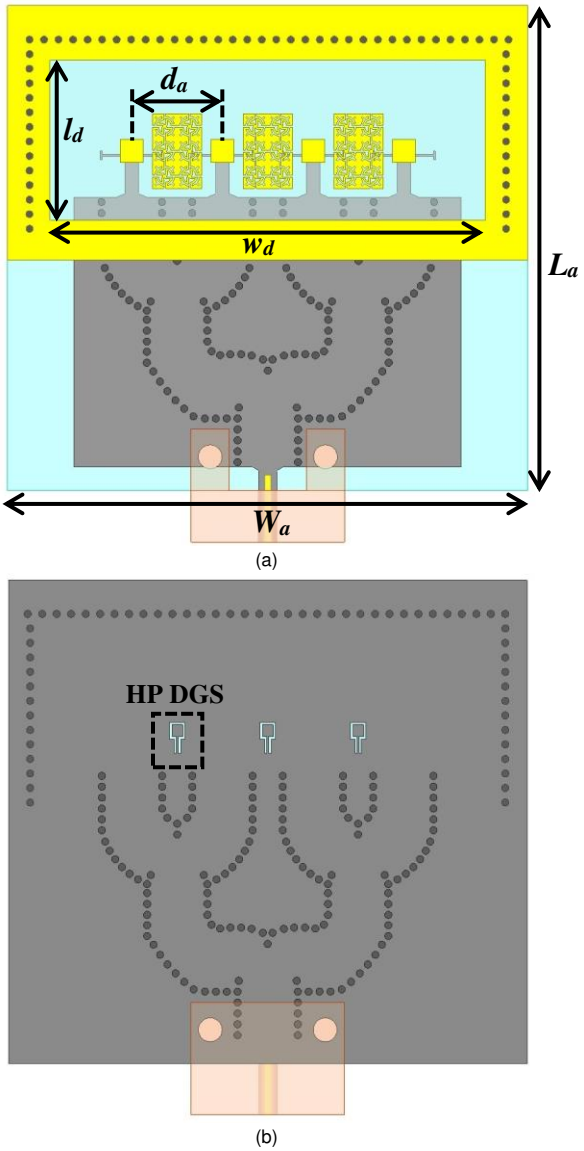

FIGURE 24. Proposed SIW cavity backed 4-element linear array loaded with EBG-DGS (a) front view (b) back view. L_a = 40, W_a = 43, l_d = 13.2, w_d = 36, d_a = 7.5 .

ports of the power divider. The front and back geometries of the proposed linear array are shown in Fig. 24. The proposed EBG and HP-DGS based hybrid decoupling elements are placed between the array elements to reduce the coupling between the adjacent antennas. Low mutual coupling between the antennas improves the overall impedance matching of the linear array. At 28 GHz the output signal amplitude at the four ports of the SIW power divider is 6.75 dB. The additional 0.75 dB loss at each output port is attributed to the effects of dielectric loss and reflection loss from the two stages T-junction dividers due to impedance mismatch. The total power radiated by 4-antennas are added in phase in the broadside direction and improve the gain of the array in H-plane. As previous, the array elements are enclosed by a SIW cavity to improve the FTBR at the resonance. The lateral dimension of the linear array is 43 × 40 mm^2 or 4.01 × 3.73 λ_0^2, where λ_0 is

This article has been accepted for publication in a future issue of this journal, but has not been fully edited. Content may change prior to final publication. Citation information: DOI 10.1109/ACCESS.2021.3133324, IEEE Access

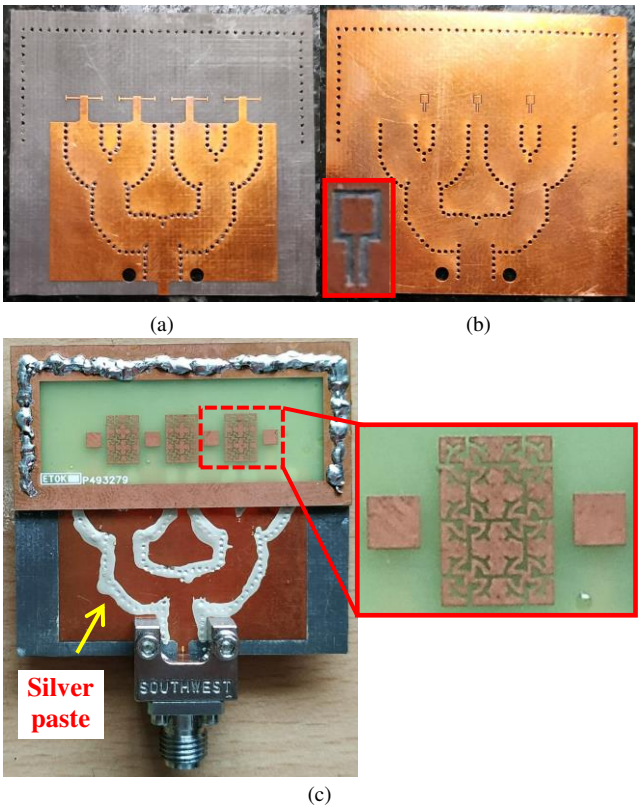

FIGURE 25. Photographs of 4 way SIW power divider (a) top view (b) bottom view (inset shows the HP-DGS) (c) Photograph of the fabricated 4-element linear array (inset shows EBG unit cells loaded radiating patches).

the wavelength at 28 GHz. A prototype of the array is also fabricated and experimentally tested. SIW power divider is made on Taconic TLY-5 substrate, whose backside is a HP-DGS integrated ground plane. The four radiating patches with three groups of 2 × 3 EBG unit cells are fabricated on FR-4 substrate. The substrate heights of Taconic TLY-5 and FR-4 are 0.51 mm and 0.8 mm respectively. Silver paste is used to fill the via holes in the structures. Photographs of the 4-way power divider and the prototype of the EBG-DGS loaded 4-element linear array are presented in Fig. 25.

B. SIMULATION AND MEASUREMENT RESULTS

The simulated and measured reflection coefficients of the linear array are depicted in Fig. 26. The resonance dip of the array occurs at 28 GHz in simulation and 27.85 GHz in measurement with the return losses are 36.3 and 33.8 dB respectively. The S_{11} of the array is compared to the EBG-DGS unloaded reference array and simulated result shows an improvement of 13.1 dB in the return loss magnitude. A small shift of resonance frequency in the measured S_{11} is present that may arise due to fabrication imperfection. Also change in relative permittivity due to use of thin layer of epoxy resin as bonding film affects the measured response of the array. The measured 10 dB return loss BW of the array covers the frequency range 27.58 to 28.17 GHz. The simulated and measured gain variations of the proposed 4-element linear

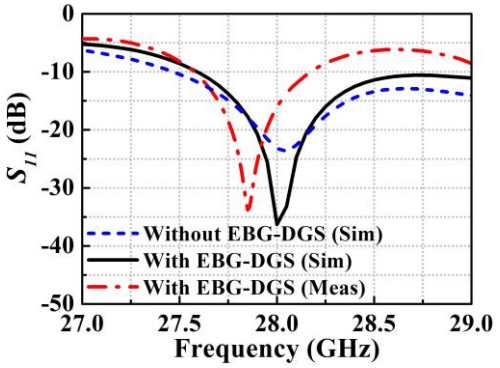

FIGURE 26. Simulated and measured reflection coefficients of the EBG-DGS loaded and unloaded 4-element linear array.

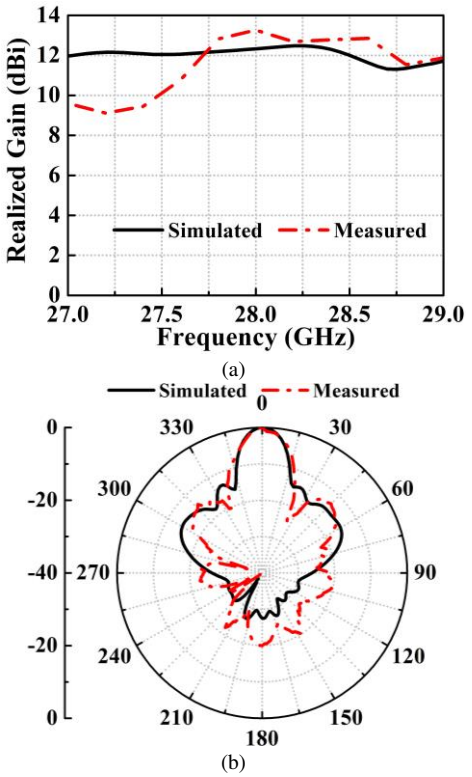

FIGURE 27. Simulated and Measured (a) gain (b) H-plane radiation patterns of the proposed EBG-DGS loaded 4-element linear array.

array are shown in Fig. 27 (a). Peak realized gain of the array at 28 GHz is 12.3 dBi in simulation and 13.3 dBi in measurement. The H-plane radiation pattern of the array at the resonance is depicted in Fig. 27 (b). The pattern shows a low sidelobe level (SLL) of 13.1 dB and FTBR of 19.97 dB in the measurement. FTBR little degrades as compared to simulated values of 27.5 dB, which may cause due to errors in the measurement. The 3 dB beamwidth of the array in H-plane is 16.2°. Fig. 28 shows the simulated and measured efficiencies of the 4-element linear array. The measured and simulated values of the efficiency are 75.9 % and 81.7 % at the operating frequency of the linear array.

This article has been accepted for publication in a future issue of this journal, but has not been fully edited. Content may change prior to final publication. Citation information: DOI 10.1109/ACCESS.2021.3133324, IEEE Access

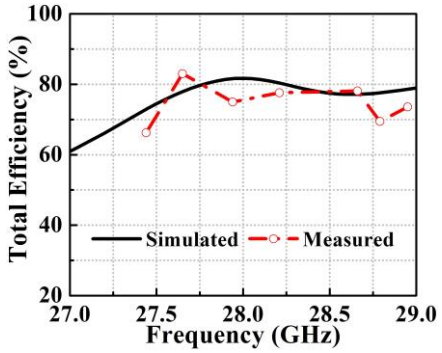

FIGURE 28. Simulated and measured efficiency of the 4-element linear array loaded with EBG and HP DGS.

VII. CONCLUSION

A novel uniplanar miniaturized EBG unit cell is designed. The proposed EBG exhibits a wideband bandgap of 20 % which has promising application for mm-wave circuit designs. This paper explores the application of EBG as a decoupling element for mutual coupling reduction in MIMO antenna. A newly proposed hair-pin shaped DGS is also included in the ground plane to further improve the isolation. The simulation and measurement results show high value of isolation over the 5G range that has potential to improve the channel capacity or beam scanning angle of the phased array. The MIMO shows the isolation of 71.9 dB between its elements with ECC value of 0.00015. The proposed MIMO antenna has the advantage of good unidirectional patterns in two principal planes with a measured peak gain of 9 dBi. The hybrid decoupling technique can be further extended for massive MIMO configuration with proper adjustment in the feed. A SIW cavity-backed 4-element linear array is also designed with EBG-DGS based decoupling elements are placed in between the antenna elements. Good radiation characteristics with low SLL, narrow beamwidth, high gain are observed for the proposed array. Indigenous designs of SIW cavity and feeding network are presented to obtain high FTBR and improved radiation patterns of the MIMO antenna and linear array, which will find application in future 5G communication at mm wave band.

ACKNOWLEDGMENT

One of the authors would like to thank the support received from the Department of Science and Technology, Govorment of India.

REFERENCES

[1] S. Kumar, A. S. Dixit, R. R. Malekar, H. D. Raut and L. K. Shevada, "Fifth generation antennas: A comprehensive review of design and performance enhancement techniques," *IEEE Access*, vol. 8, pp. 163568-163593, Sep. 2020.

[2] W. Hong *et al*., "Multibeam antenna technologies for 5G wireless communications," *IEEE Trans. Antennas Propag.*, vol. 65, no. 12, pp. 6231-6249, Dec. 2017.

[3] H. J. Song, A. Bekaryan, J. H. Schaffner, A. Hussain and P. Kildal, "Effects of mutual coupling on LTE MIMO capacity for monopole array: comparing reverberation chamber tests and drive tests," *IEEE Antennas Wireless Propag. Lett.*, vol. 14, pp. 454-457, Nov. 2014.

[4] M. Kiani-Kharaji, H. R. Hassani, and S. Mohammad-Ali-Nezhad, "Wide scan phased array patch antenna with mutual coupling reduction," *IET Microw. Antennas Propag.*, vol. 12, no. 12, pp. 1932–1938, Sep. 2018.

[5] K. S. Vishvaksenan, K. Mithra, R. Kalaiarasan, and K. S. Raj, "Mutual coupling reduction in microstrip patch antenna arrays using parallel coupled-line resonators," *IEEE Antennas Wireless Propag. Lett.*, vol. 16, pp. 2146–2149, May 2017.

[6] Y. Wang and Z. Du, "A wideband printed dual-antenna with three neutralization lines for mobile terminals," *IEEE Trans Antennas Propag.*, vol. 62, no. 3, pp. 1495-1500, Mar. 2014.

[7] S. Zhang and G. F. Pedersen, "Mutual coupling reduction for UWB MIMO antennas with a wideband neutralization line," *IEEE Antennas Wireless Propag. Lett.*, vol. 15, pp. 166-169, Feb. 2016.

[8] Y.-F. Cheng, X. Ding, W. Shao, and B.-Z. Wang, "Reduction of mutual coupling between patch antennas using a polarization-conversion isolator," *IEEE Antennas Wireless Propag. Lett.*, vol. 16, pp. 1257–1260, Nov. 2016.

[9] A. Jafargholi, A. Jafargholi, and J. H. Choi, "Mutual coupling reduction in an array of patch antennas using cll metamaterial superstrate for mimo applications," *IEEE Trans. Antennas Propag.*, vol. 67, no. 1, pp. 179–189, Oct. 2018.

[10] Z. Wang, L. Zhao, Y. Cai, S. Zheng, and Y. Yin, "A meta-surface antenna array decoupling (maad) method for mutual coupling reduction in a mimo antenna system," *Scientific reports*, vol. 8, no. 1, pp. 1–9, Feb. 2018.

[11] H. Luan, C. Chen, W. Chen, L. Zhou, H. Zhang, and Z. Zhang, "Mutual coupling reduction of closely e/h-plane coupled antennas through metasurfaces," *IEEE Antennas Wireless Propag. Lett.*, vol. 18, no. 10, pp. 1996–2000, Aug. 2019.

[12] M. Li, B. G. Zhong and S. W. Cheung, "Isolation enhancement for MIMO patch antennas using near-field resonators as coupling-mode transducers," *IEEE Trans. Antennas Propag.*, vol. 67, no. 2, pp. 755-764, Feb. 2019.

[13] Z. Qamar, U. Naeem, S. A. Khan, M. Chongcheawchamnan, and M. F. Shafique, "Mutual coupling reduction for high-performance densely packed patch antenna arrays on finite substrate," *IEEE Trans. Antennas Propag.*, vol. 64, no. 5, pp. 1653–1660, Feb. 2016.

[14] J.-Y. Lee, S.-H. Kim, and J.-H. Jang, "Reduction of mutual coupling in planar multiple antenna by using 1-d ebg and srr structures," *IEEE Trans. Antennas Propag.*, vol. 63, no. 9, pp. 4194–4198, Jun. 2015.

[15] F. Yang and Y. Rahmat-Samii, "Microstrip antennas integrated with electromagnetic band-gap (ebg) structures: A low mutual coupling design for array applications," *IEEE Trans. Antennas Propag.*, vol. 51, no. 10, pp. 2936–2946, Oct. 2003.

[16] M. Coulombe, S. F. Koodiani, and C. Caloz, "Compact elongated mushroom (em)-ebg structure for enhancement of patch antenna array performances," *IEEE Trans. Antennas Propag.*, vol. 58, no. 4, pp. 1076–1086, Jan. 2010.

[17] S. Ghosh, T.-N. Tran, and T. Le-Ngoc, "Dual-layer ebg-based miniaturized multi-element antenna for mimo systems," *IEEE Trans. Antennas Propag.,* vol. 62, no. 8, pp. 3985–3997, May 2014.

[18] X. Yang, Y. Liu, Y. Xu, and S. Gong, "Isolation enhancement in patch antenna array with fractal UC-EBG structure and cross slot," *IEEE Antennas Wireless Propag. Lett.*, vol. 16, pp. 2175-2178, May 2017.

[19] S. D. Assimonis, T. V. Yioultsis, and C. S. Antonopoulos, "Design and optimization of uniplanar ebg structures for low profile antenna applications and mutual coupling reduction," *IEEE Trans. Antennas Propag.*, vol. 60, no. 10, pp. 4944–4949, Jul. 2012.

[20] Z. Qamar, U. Naeem, S. A. Khan, M. Chongcheawchamnan, and M. F. Shafique, "Mutual coupling reduction for high-performance densely packed patch antenna arrays on finite substrate," *IEEE Trans. Antennas Propag.*, vol. 64, no. 5, pp. 1653–1660, Feb. 2016.

[21] X. Tan, W. Wang, Y. Wu, Y. Liu and A. A. Kishk, "Enhancing isolation in dual-band meander-line multiple antenna by employing split EBG structure," *IEEE Trans. Antennas Propag.*, vol. 67, no. 4, pp. 2769-2774, Apr. 2019.

[22] Y. Liu, X. Yang, Y. Jia, and Y. J. Guo, "A low correlation and mutual coupling mimo antenna," IEEE Access, vol. 7, pp. 127 384–127 392, Sep. 2019.

[23] S. Hwangbo, H. Y. Yang, and Y.-K. Yoon, "Mutual coupling reduction using micromachined complementary meander-line slots for

a patch array antenna," *IEEE Antennas Wireless Propag. Lett.*, vol. 16, pp. 1667–1670, Feb. 2017.

[24] K. Wei, J.-Y. Li, L. Wang, Z.-J. Xing, and R. Xu, "Mutual coupling reduction by novel fractal defected ground structure bandgap filter," *IEEE Trans. Antennas Propag.*, vol. 64, no. 10, pp. 4328–4335, Jul. 2016.

[25] P. Garg and P. Jain, "Isolation improvement of MIMO antenna using a novel flower shaped metamaterial absorber at 5.5 GHz WiMAX band," *IEEE Trans. Circuits Syst. II, Exp. Briefs*, vol. 67, no. 4, pp. 675-679, Apr. 2020

[26] D. Pozar, "Considerations for millimeter wave printed antennas," *IEEE Trans. Antennas Propag.*, vol. 31, no. 5, pp. 740-747, Sep. 1983.

[27] Jong-Gwan Yook and L. P. B. Katehi, "Micromachined microstrip patch antenna with controlled mutual coupling and surface waves," *IEEE Trans. Antennas Propag.*, vol. 49, no. 9, pp. 1282-1289, Sept. 2001.

[28] X. Chen, M. Abdullah, Q. Li, J. Li, A. Zhang and T. Svensson, "Characterizations of mutual coupling effects on switch-based phased array antennas for 5G millimeter-wave mobile communications," *IEEE Access*, vol. 7, pp. 31376-31384, Mar. 2019.

[29] J. Mu'ath, T. A. Denidni, and A. R. Sebak, "Millimeter-wave compact ebg structure for mutual coupling reduction applications," *IEEE Trans. Antennas Propag.*, vol. 63, no. 2, pp. 823–828, Dec. 2014.

[30] I. B. Mabrouk, R. E'qab, M. Nedil, T. A. Denidni et al., "Hybrid isolator for mutual-coupling reduction in millimeter-wave mimo antenna systems," *IEEE Access*, vol. 7, pp. 58 466–58 474, May 2019.

[31] R. Selvaraju, M. H. Jamaluddin, M. R. Kamarudin, J. Nasir, and M. H. Dahri, "Mutual coupling reduction and pattern error correction in a 5g beamforming linear array using csrr," *IEEE Access*, vol. 6, pp. 65 922–65 934, Oct. 2018.

[32] S. Gupta, Z. Briqech, A. R. Sebak, and T. A. Denidni, "Mutual-coupling reduction using metasurface corrugations for 28 ghz mimo applications," *IEEE Antennas Wireless Propag. Lett*., vol. 16, pp. 2763–2766, Aug. 2017.

[33] Y. Zhang, J.-Y. Deng, M.-J. Li, D. Sun, and L.-X. Guo, "A mimo dielectric resonator antenna with improved isolation for 5g mm-wave applications," *IEEE Antennas Wireless Propag. Lett.*, vol. 18, no. 4, pp. 747–751, Feb. 2019.

[34] R. Karimian, A. Kesavan, M. Nedil and T. A. Denidni, "Low-mutual-coupling 60-GHz MIMO antenna system with frequency selective surface wall," *IEEE Antennas Wireless Propag. Lett.*, vol. 16, pp. 373-376, Mar. 2017.

[35] D. Sievenpiper, Lijun Zhang, R. F. J. Broas, N. G. Alexopolous and E. Yablonovitch, "High-impedance electromagnetic surfaces with a forbidden frequency band," *IEEE Trans. Microw. Theory Techn.*, vol. 47, no. 11, pp. 2059-2074, Nov. 1999.

[36] R. Garg, I. Bahl, and M. Bozzi, Microstrip lines and slotlines, 2nd ed. *Artech house*, 2013.

[37] X. Chen, T. M. Grzegorczyk, B.-I. Wu, J. Pacheco Jr, and J. A. Kong, "Robust method to retrieve the constitutive effective parameters of metamaterials," *Physical review E*, vol. 70, no. 1, p. 016608, Jul. 2004.

[38] C. A. Balanis, *Antenna Theory: Analysis and Design*. Hoboken, NJ, USA: Wiley, 2016.

[39] J. S. Hong and M. J. Lancaster, Microstrip Filter for RF/Microwave Application, New York: Wiley, 2001.

[40] A. A. Ghannad, M. Khalily, P. Xiao, R. Tafazolli, and A. A. Kishk, "Enhanced matching and vialess decoupling of nearby patch antennas for mimo system," *IEEE Antennas Wireless Propag. Lett*., vol. 18, no. 6, pp. 1066–1070, Mar. 2019.

[41] D. Agahi and W. Domino, "Efficiency measurements of portable-handset antennas using the wheeler cap," *Applied Microw. Wireless*, vol. 12, no. 6, pp. 34–43, 2000.

[42] H. N. Chen, J. Song and J. Park, "A compact circularly polarized MIMO dielectric resonator antenna over electromagnetic band-gap surface for 5G applications," *IEEE Access*, vol. 7, pp. 140889-140898, Sep. 2019.